



Fabrication of highly efficient g-C₃N₄/ZnO/Fe₂O₃ ternary composite with enhanced photocatalytic activity under visible light irradiation

K. Shanthini^{1,2}, V. Manivannan^{1,*}, K. M. Govindaraju³, V. Collins Arun Prakash⁴, G. S. Lekshmi^{5,*}, and R. Govindan^{6,*} 

¹Department of Chemistry, Thiruvalluvar Government Arts College, Rasipuram 637401, India

²Department of Chemistry, Padmavani Arts & Science College for Women, Salem 636011, India

³Department of Chemistry, PSG College of Arts and Science, Coimbatore 641014, India

⁴Department of Chemistry, Sacred Heart College (Autonomous), Tirupattur 635601, India

⁵Centre for Nanoscience and Technology, AC College of Technology, Anna University, Chennai 600025, India

⁶Key Laboratory of Theoretical Chemistry of Environment, Ministry of Education, School of Chemistry, South China Normal University, Guangzhou 510006, People's Republic of China

Received: 11 January 2022

Accepted: 19 May 2022

Published online:

5 June 2022

© The Author(s), under exclusive licence to Springer Science+Business Media, LLC, part of Springer Nature 2022

ABSTRACT

The development of an efficient and photostable heterostructured photocatalyst has attracted a great deal of attention for the degradation of organic pollutants under visible light. Herein, we have developed a highly efficient graphitic carbon nitride/zinc oxide/iron oxide (g-C₃N₄/ZnO/Fe₂O₃) ternary composite photocatalysts that were prepared by a simple and cost-effective calcination method. The crystalline structure, functional groups, morphological and optical properties of the as-prepared g-C₃N₄/ZnO/Fe₂O₃ (GZF) ternary composite were characterized by X-ray diffraction, Fourier transform infrared spectroscopy, scanning electron microscopy and UV–Vis diffuse-reflectance spectroscopic techniques. The GZF composite reveals enhanced methylene blue (MB) degradation with good photostability of 100% retention rate even after 5 cycles under visible light irradiation. Moreover, GZF composite was degraded 94% of MB after 120 min under visible light irradiation which was almost 6.6- and 3.1-fold higher than individual g-C₃N₄ (GCN) and g-C₃N₄/ZnO (GZ). The results suggest that the composites of g-C₃N₄ with metal oxide under visible light significantly enhance the electron transfer process.

Address correspondence to E-mail: vmanivannan07@gmail.com; lekshmidhanooj@gmail.com; en2sci@gmail.com

1 Introduction

The development of heterogeneous nanomaterials as photocatalysts has attracted a greater attention in environmental and energy applications [1, 2]. Particularly, due to its outstanding charge transferring ability of these semiconductor nanomaterials, they have been extensively employed as a competent photocatalyst for degradation of organic dyes under UV as well as visible light irradiation [3–5]. However, the moderate ion conductivity, rapid ion recombination, inadequate light absorption and poor visible light responses of these semiconductor photocatalysts restrict its practical application. Therefore various strategies have been tried to overcome these shortcomings and improve the photocatalytic performances of the semiconductor-based heterogeneous photocatalysts. Recently, graphitic carbon nitride ($g\text{-C}_3\text{N}_4$), a two-dimensional (2D) n-type metal-free polymeric semiconductor material was widely studied for environmental application due to its excellent chemical stability, low-cost, non-toxicity and significant optical bandgap (2.7–2.8 eV) [6–8]. However, pure $g\text{-C}_3\text{N}_4$ as photocatalysts has restricted its photocatalytic activity owing to its reduced electron conductivity, poor visible light absorption and quick charge recombination [9]. Henceforth, it is essential to reduce the electron–hole recombination of $g\text{-C}_3\text{N}_4$ [10].

Dyes are organic compounds and considered as common pollutants in wastewaters which are widely used in textiles, cosmetics, food, printing, plastics, and leather industries. Moreover, some dyes are toxic and hazardous which cannot undergo biodegradation naturally [11]. Predominantly, Methylene blue (MB) is a cationic dye and used broadly in the textile industry and as a contaminant in water system and can cause vomiting, diarrhoea, nausea and a burning sensation in the eyes [12]. Hence, it is necessary to remove this dye from water system using low-cost photocatalysts. In recent years, various metal oxides and metal sulfides have been integrated with $g\text{-C}_3\text{N}_4$ to enhance the photocatalytic performance of the $g\text{-C}_3\text{N}_4$ and showed outstanding photocatalytic performance than individual counterparts [10–19]. Particularly, zinc oxide (ZnO) with an energy gap of 3.37 eV has attracted enormous attention owing to its high excitation-binding energy of 60 meV, inexpensive and non-toxic in nature and has resulted in high stability and outstanding photocatalytic activity

[20–22]. For instance, Gayathri et al., had reported ZnO/ $g\text{-C}_3\text{N}_4$ hybrids for the degradation of different organic dyes and showed enhanced photocatalytic activity towards methylene blue and Acid blue 113 dyes with the percentage degradation of 97 and 83% at 90 and 120 min irradiation, respectively [23]. Nevertheless, the application of $g\text{-C}_3\text{N}_4/\text{ZnO}$ composite is limited owing to the poor absorption of the visible light region in the solar spectrum, which can be overcome by the fabrication of composite with magnetic iron oxides that can increase the photocatalytic properties of $g\text{-C}_3\text{N}_4/\text{ZnO}$ in the visible light region [24–27]. Wang et al., have synthesized $\text{Fe}_3\text{O}_4/\text{ZnO}/g\text{-C}_3\text{N}_4$ nanocomposite for the photodegradation of Rhodamine B under visible light irradiation [28]. The as-prepared $\text{Fe}_3\text{O}_4/\text{ZnO}/g\text{-C}_3\text{N}_4$ nanocomposite displayed outstanding photocatalytic performance with a degradation efficiency of 100% even after 150 min irradiation to visible light.

Herein, $g\text{-C}_3\text{N}_4/\text{ZnO}/\text{Fe}_2\text{O}_3$ (GZF) ternary composite has been prepared by direct calcination method because it is considered as an efficient method for large-scale production [29] and its degradation performance toward MB dye in an aqueous medium was evaluated. The prepared GZF composite exhibits an enhanced degradation rate than pristine $g\text{-C}_3\text{N}_4$, which is due to the combined effect of $g\text{-C}_3\text{N}_4$ and metal oxide nanoparticles. Especially, the GZF composite can effectively degrade the dye constantly and holds high stability.

2 Experimental details

2.1 Materials

Melamine ($\text{C}_3\text{H}_6\text{N}_6$, 99%), zinc oxide (ZnO, 99%) and ferric oxide (Fe_2O_3 , 98%) nanoparticles were purchased from Alfa Aesar, Merck India and Nice Chemicals India, respectively, and were used without any further purification. Ethanol (EtOH, $\text{C}_2\text{H}_5\text{OH}$, 99%) was used as the solvent for the preparation of photocatalysts.

2.2 Synthesis of $g\text{-C}_3\text{N}_4$ (GCN), $g\text{-C}_3\text{N}_4/\text{ZnO}$ (GZ) and $g\text{-C}_3\text{N}_4@/\text{ZnO}@/\text{Fe}_2\text{O}_3$ (GZF)

To prepare $g\text{-C}_3\text{N}_4$, pre-weighted melamine was transferred into a partially covered alumina crucible

and heated in a muffle furnace at 550 °C for 4 h with a heating rate of 2 °C/min in air atmosphere condition. Then, it was allowed to cool to room temperature and the obtained yellow product was grounded with agate mortar into a fine powder which is named as GCN. For the synthesis of g-C₃N₄/ZnO composite, 0.5 g of g-C₃N₄ was dispersed into 50 mL of ethanol using ultrasonicator for 30 min. Then, 0.05 g of ZnO nanoparticles was added to the above dispersion and ultrasonicated for 10 min followed by vigorous stirring at room temperature for 24 h. The obtained mixture was dried and heat-treated at 450 °C for 2 h in a muffle furnace. Finally, the g-C₃N₄/ZnO hybrid was obtained (labeled as GZ).

To prepare GZF composite, 0.5 g of g-C₃N₄ was dispersed into 50 mL of ethanol using ultrasonicator for 30 min. Then, 0.05 g of ZnO nanoparticles and 0.005 g of Fe₂O₃ nanoparticles were added to the above dispersion and ultrasonicated for 10 min followed by vigorous stirring at room temperature for 24 h. The obtained mixture was dried and heat-treated at 450 °C for 2 h in a muffle furnace and which was labeled as GZF.

2.3 Characterization

The X-ray diffraction (XRD, Rigaku Miniflex II X-ray diffractometer) analysis was performed to identify the crystalline nature of samples. The functional groups and chemical bonds were recognized by Fourier Transform Infrared spectroscopy (FTIR, Bruker Tensor27 instrument) with KBr as reference material. The morphology of the prepared samples was imaged by Scanning Electron Microscopy (SEM, Zeiss Gemini, Japan). Elements present in the sample was confirmed with an energy-dispersive X-ray spectroscope (EDX, Oxford Instrument). The absorption spectra in DRS mode were acquired using Analytek Jena spectrophotometer. N₂ adsorption/desorption analysis (Quantachrome Instruments) was used to calculate the Brunauer–Emmett–Teller (BET) surface area and Barrett–Joyner–Halenda (BJH) pore size distribution. Photoluminescence (PL) measurements were carried out using Varian Cary Eclipse Fluorescence spectrometer at room temperature.

2.4 Photocatalytic performance

The photocatalytic performance of prepared GCN, GZ, and GZF composites was evaluated by observing the degradation of an MB under visible light using a 350 W Xe lamp with 420 nm cut-off the filter as a light source. To study the photocatalytic performance of samples, 50 mg of catalyst was dispersed into 50 mL (30 mg/L) of MB solution and stirred for 1 h under the dark conditions at room temperature to achieve adsorption equilibrium. Then the mixed solution was irradiated under Xe lamp. Blank solution (without catalyst) was also subjected under the same condition. During the photocatalytic degradation, 2 mL of solution was withdrawn at every 15 min intervals and centrifuged to isolate the catalyst. The photocatalytic dye degradation efficiency was assessed by observing the change in the wavelength value of MB at 664 nm using UV–Vis spectrophotometer. Total organic carbon (TOC) removal efficiency was calculated by Analytikjena/multi N/C 3100.

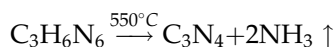
The change in dye concentration was represented by C/C_0 and dye degradation percent (D_p) was calculated using the following equation,

$$\text{Degradation percent } (D_p) = [1 - (C/C_0)] \times 100\%,$$

where C_0 and C are the initial concentration and the persisted concentration of MB.

3 Results and discussion

The raw material, Melamine, can be thermally pyrolysed under an air atmosphere to form C₃N₄ and NH₃. The reaction equation is,



The g-C₃N₄ was prepared under controlled heating conditions. Initially, the raw material melamine was transferred into an alumina crucible with a partially covered lid and kept into a muffle furnace. Then the melamine was heated at 550 °C for 4 h with heating rate of 2 °C/min and the yellow colored g-C₃N₄ (GCN) powder was obtained. To prepare GZ, the as-prepared GCN was added to ethanol and ultrasonicated until complete dispersion. Then the calculated amount of commercially available ZnO nanoparticles was mixed into above GCN dispersion and further ultrasonicated followed by stirring for 24 h. Then the

obtained GCN/ZnO complex was heat-treated at 450 °C for 2 h. For the preparation of GZF, pre-determined amounts of ZnO and Fe₂O₃ nanoparticles were added in to the GCN/ethanol dispersion and stirred for 24 h. The final product was heat-treated at 550 °C for 2 h.

The X-ray diffraction patterns of the as-prepared GCN, GZ and GZF GZF are displayed in Fig. 1a. The XRD pattern of pure GCN revealed two diffraction peaks at 27.5° and 13.1°, which corresponds to (002) and (100) planes, respectively [30]. The diffraction peaks detected in GZ composite at 2θ values of 31.4°, 34.10°, 36.02°, 47.26°, 56.39°, 62.56°, 66.02°, 67.61°, 68.79°, 72.08°, and 76.64°, are assigned to (100), (002), (101), (102), (110), (103), (200), (112), (201), (004), and (202) lattice planes of the hexagonal structure of ZnO and which are well-matched with standard JCPDS No. 89-7102. Nevertheless, the diffraction peaks of ZnO were slightly shifted to lower theta values compared to JCPDS values, which is due to the presence of g-C₃N₄ in the GZ composite structure [31]. Moreover, the additional peak at 27.5° was observed in GZ, which confirms the presence of g-C₃N₄ and ZnO in the GZ composite material. The XRD pattern of GZF composite displays the additional peaks at 29.9, 35.1, 43.1, and 62.3° along with diffraction peaks of ZnO and g-C₃N₄ which corresponds to (220), (311), (400), and (440) lattice planes of Fe₂O₃ and these peaks well-matches with the standard JCPDS (39-1346). In addition, the intensity of diffraction peaks of GZF composite had decreased compared to GZ which confirms the existence of Fe₂O₃ in the GZF composite [32].

The functional groups present in g-C₃N₄, ZnO, and Fe₂O₃ in the GCN, GZ, and GZF and the interaction between a metal oxide and g-C₃N₄ can be confirmed by FTIR spectra displayed in Fig. 1b. As seen in Fig. 1b, the FTIR spectra of pure g-C₃N₄ contained characteristics peaks at 3760, 1635, 1560, 1402, 1326, 1247, 881, and 810 cm⁻¹. The bands at 3000–3300 cm⁻¹ are ascribed to the N–H stretching vibrations of the amino groups [33]. The vibrational peaks that appear at 1635 and 1560 cm⁻¹ are attributed to the C=N bonds of heterocyclic rings [34]. In addition, the characteristic peaks observed at 1402, 1326, and 1247 cm⁻¹ belong to the stretching vibrations of aromatic C–N heterocycles [35]. The characteristic bands observed at 810 and 881 cm⁻¹, corresponds to the tris-triazine or heptazine units and the deformation of N–H vibrations, respectively [36]. Moreover, the small vibration peak at 3760 cm⁻¹ can be ascribed to the –OH group due to adsorbed H₂O molecule. The FTIR spectrum of GF displays new bands at 503, 692, and 921 cm⁻¹ along with characteristic peaks of g-C₃N₄ which could be due to the stretching vibrations of Zn–O and Zn–OH. In case of GZF composite, additional vibration peaks appeared at 931 cm⁻¹ which corresponds to the stretching vibration of Fe–OH, and peaks at 669, 503, and 437 cm⁻¹ are ascribed to the stretching vibrations of Fe–O [37]. Interestingly, after the incorporation of metal oxide with g-C₃N₄, the intensity and peak broadening as well as peak shifts were observed, which indicates that the metal oxides successfully alter chemical bonding that enhances the electron–hole charge carriers.

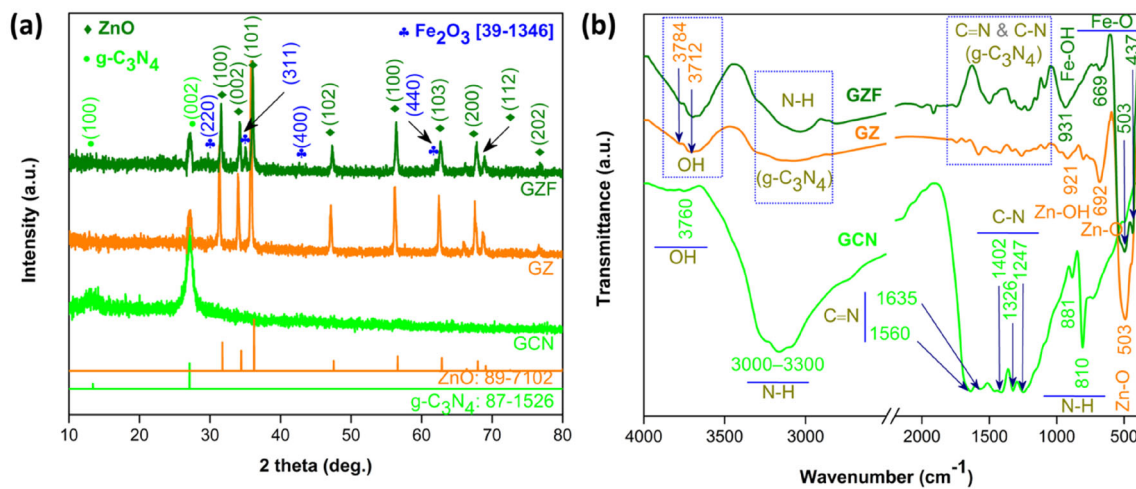


Fig. 1 **a** XRD patterns and **b** FTIR spectra of GCN, GZ and GZF

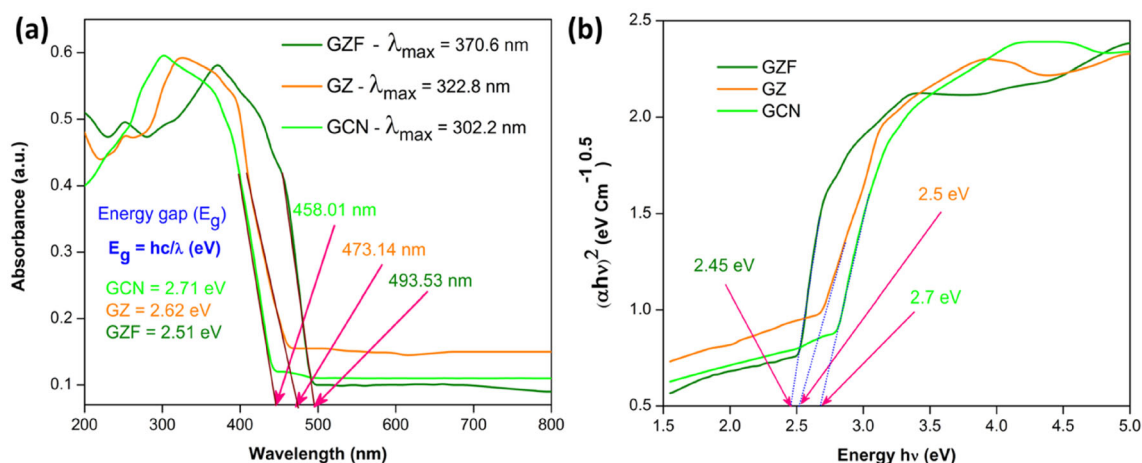


Fig. 2 **a** UV-Vis-DRS and **b** Energy gap plot for GCN, GZ and GZF

The optical characteristic feature and bandgap energy of the synthesized GCN, GZ, and GZF was studied by UV-Vis-DRS and the results are presented in Fig. 2a. As shown in Fig. 2a, the adsorption edge of GCN was observed at 458 nm which corresponds to the energy gap at 2.71 eV [38]. Meanwhile, the adsorption edge of GZ (473.14 nm) and GZF (493.53 nm) revealed robust light absorption as well as redshift of absorption edge and their corresponding band gaps are 2.63 and 2.51 eV, respectively. This redshift of adsorption showed the improvement of photo-induced electrons and holes charge carriers which enhance the photocatalytic performance [39]. As shown in Fig. 2b, the band gap energy of pure $g\text{-C}_3\text{N}_4$ is 2.7 eV which matches well with an earlier report [40]. The bandgap energies of GZ and GZF decreased to 2.5 eV and 2.45 eV, respectively, which clearly indicates the semiconductor material effectively reduce the energy gap of the composite. Moreover, photogenerated electron-hole charge carriers of $g\text{-C}_3\text{N}_4$ were enhanced with the addition ZnO and Fe_2O_3 which agreed with the previous investigation [24].

The PL spectra was further used to investigate the charge separation and charge recombination processes of the photoinduced electron-hole pairs [41]. It was found that the PL intensity is in proportion with the rate of recombination of the photoinduced electron-hole pairs. Figure 3 shows the PL spectra of GCN, GZ, and GZF samples performed at an excitation wavelength of 365 nm. The PL results clearly indicate that the GCN reveals a strong PL intensity at 460 nm owing to $n\text{-}\pi^*$ transition in GCN [42], representing faster recombination of a photogenerated

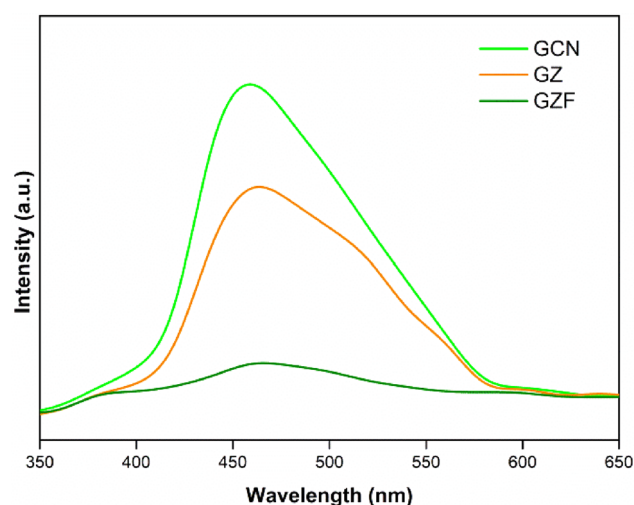


Fig. 3 Photoluminescence (PL) emission spectra of GCN, GZ and GZF

electrons with the holes. The GZ sample exhibits lower PL peak intensity, suggesting more effective charge transport pathway formed by combining $g\text{-C}_3\text{N}_4$ with ZnO [43]. It is noteworthy that, GZF displays very low PL intensity compared to GCN and GZ, clearly indicating that lower rate of recombination of photogenerated electron-hole pair resulted in enhanced photodegradation of MB dyes in aqueous medium.

The morphology and macro-structure of the GCN, GZ, and GZF were imaged by SEM (Fig. 4). GCN sample was evidently seen in micrometer size with aggregation and it consists of a large number of sheets which were dense stacked-layer-like structure. The SEM image of GZ displays the presence of hexagonal ZnO microparticles (red arrow) along

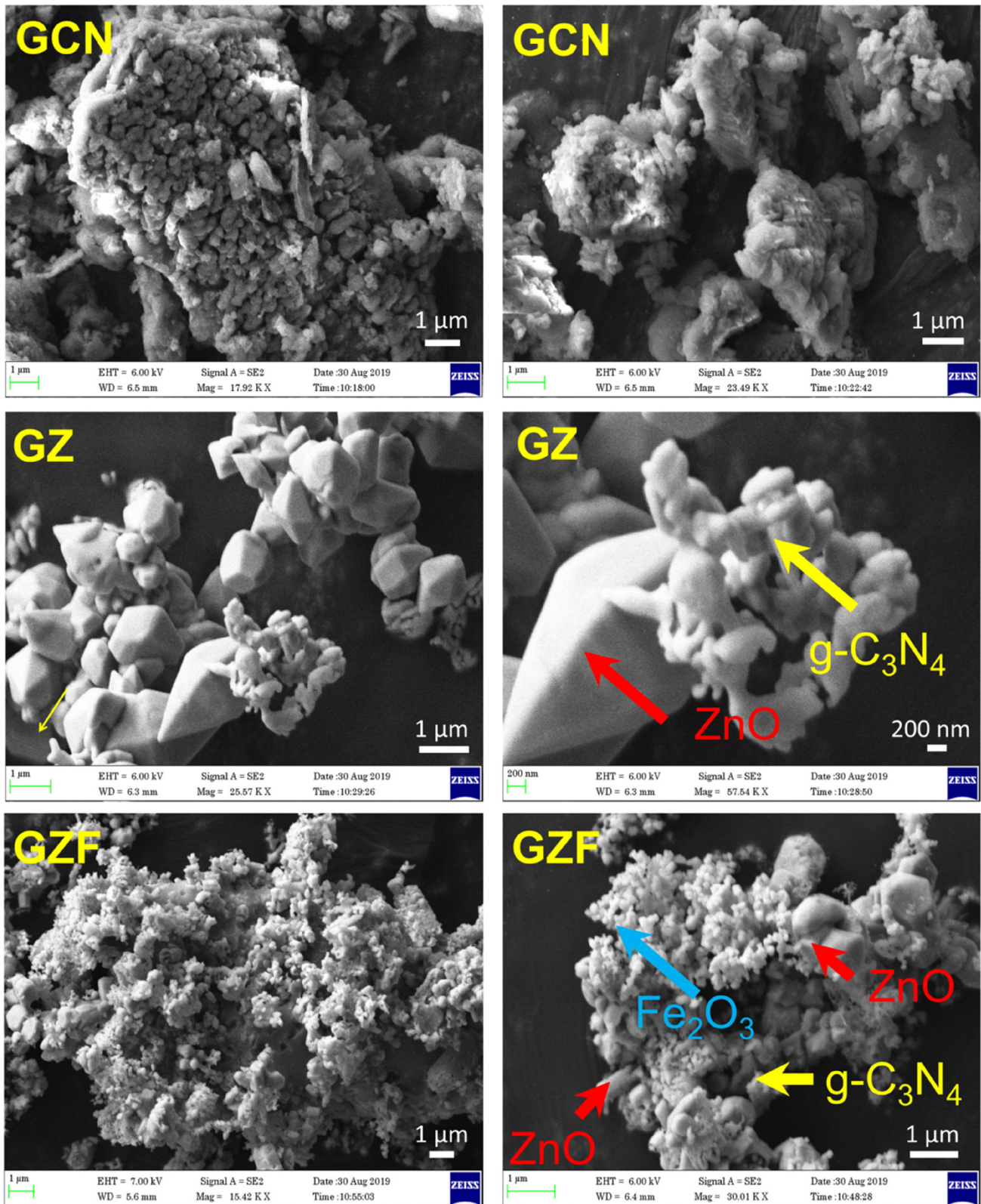


Fig. 4 SEM morphology of GCN, GZ and GZF

with aggregated g-C₃N₄ (yellow arrow). The size of the ZnO particles was in the range of 200–1000 nm. The SEM images of GZF clearly indicates the existence of Fe₂O₃ (blue arrow) nanoparticles along with ZnO and g-C₃N₄. It can be observed that the size of the Fe₂O₃ nanoparticles in the GZF composite is approximately 50–150 nm.

The EDS analysis of the GCN, GZ, and GZFs samples confirm the elements present in the composites. Figure 5a shows the EDS spectra and corresponding weight as well atomic percentage of GCN, GZ, and GZF. The EDS analysis confirmed the existence of C, N, Zn, O, and Fe in the GZF composite. Nevertheless, in GZ composite, C, N, Zn, and O elements were observed whereas C and N were found in the case of GCN.

Importantly, no additional elements were observed except C, N, Zn, O, and Fe in the GZF composite which confirms the purity of the composite. The EDS analysis clearly indicates that the presence of all the elements which were used in the sample preparation. Moreover, the weight and atomic percentage of Fe in the GZF composite are 2.45% and 0.71%, respectively, which were very small compared to other elements.

Photocatalysts with greater specific surface areas provide more active sites which is favorable for the improvement of photocatalytic performance under visible light irradiation. However, this is not the case with the GCN composite system. The specific surface area and pore distribution of GCN, GZ, and GZF were measured by N₂ adsorption/desorption isotherms which are displayed in Fig. 6a. The N₂ isotherms for the GCN, GZ, and GZF revealed typical type IV isotherms with type H3 hysteresis loops, representing the existence of both mesopores and

macropores in the prepared samples [44]. The BET surface area of GCN, GZ, and GZF was 25.5, 42.8, and 51.4 m²/g, respectively. Besides, the pore size distributions of the GCN, GZ, and GZF was calculated from the BJH method (Fig. 6b) and found to be from 2 to 30 nm, demonstrating that the existence of meso-to macropores. The high surface area and existence of meso/macro pores of GZF hybrid provide more active sites thus enhances the photocatalytic activity against MB degradation in an aqueous medium.

The elemental composition and valance of the GFZ composite was further confirmed by XPS analysis [45]. Figure 7a shows the XPS survey spectrum of GFZ composite and mainly comprises C, N, O, Zn, and Fe. For C 1s scan spectrum (Fig. 7b), three distinguishable peaks were observed at 284.8 and 288.1 eV. The peak at 284.8 eV, corresponds to the C–C bond with sp² hybridization whereas the peak at 288.1 eV denotes the occurrence of sp²-bonded C–N=H from the aromatic rings of g-C₃N₄ [46, 47]. The N 1s scan spectrum (Fig. 7c) showed four peaks at 398.7, 399.4, 401.4, and 404.8 eV. The peak at 398.7 eV is related to sp² hybridized C=N–C group in the triazine rings, while peak at 399.4 eV could be ascribed to the tertiary nitrogen bonded to carbon (N–(C)3) links the basic (C₆N₇) structure [32]. The other two peaks at 401.4 and 404.8 eV are attributed to amino-functional groups (C–N–H), and charging effects in heterocycles [48, 49]. The Zn 2p spectrum (Fig. 7d) reveals two distinguish peaks at 1022.5 and 1045.7 eV, which are associated with the binding energy of Zn 2p_{3/2} and Zn 2p_{1/2}, respectively, confirming the characteristic Zn–O bonds [50]. The distance between the two zinc peaks is found to be 23.2 eV, suggesting that the zinc ion in the GZF

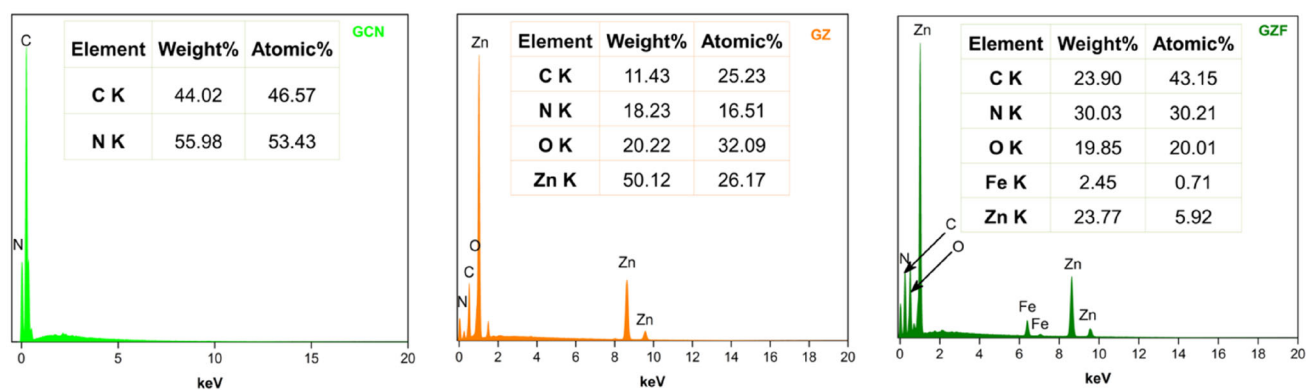


Fig. 5 EDS spectra of GCN, GZ, and GZF

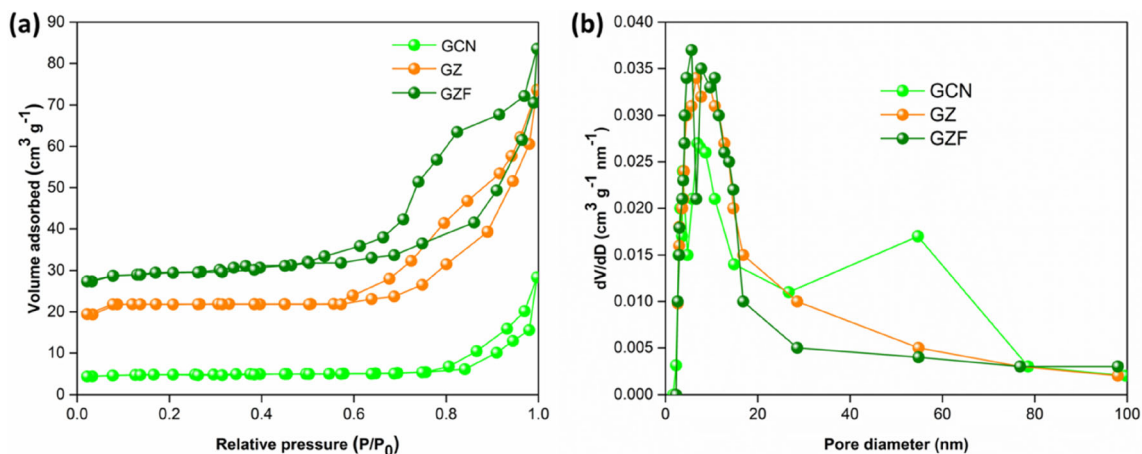


Fig. 6 **a** N₂ adsorption–desorption isotherms and **b** BJH pore size distribution of GCN, GZ, and GZF

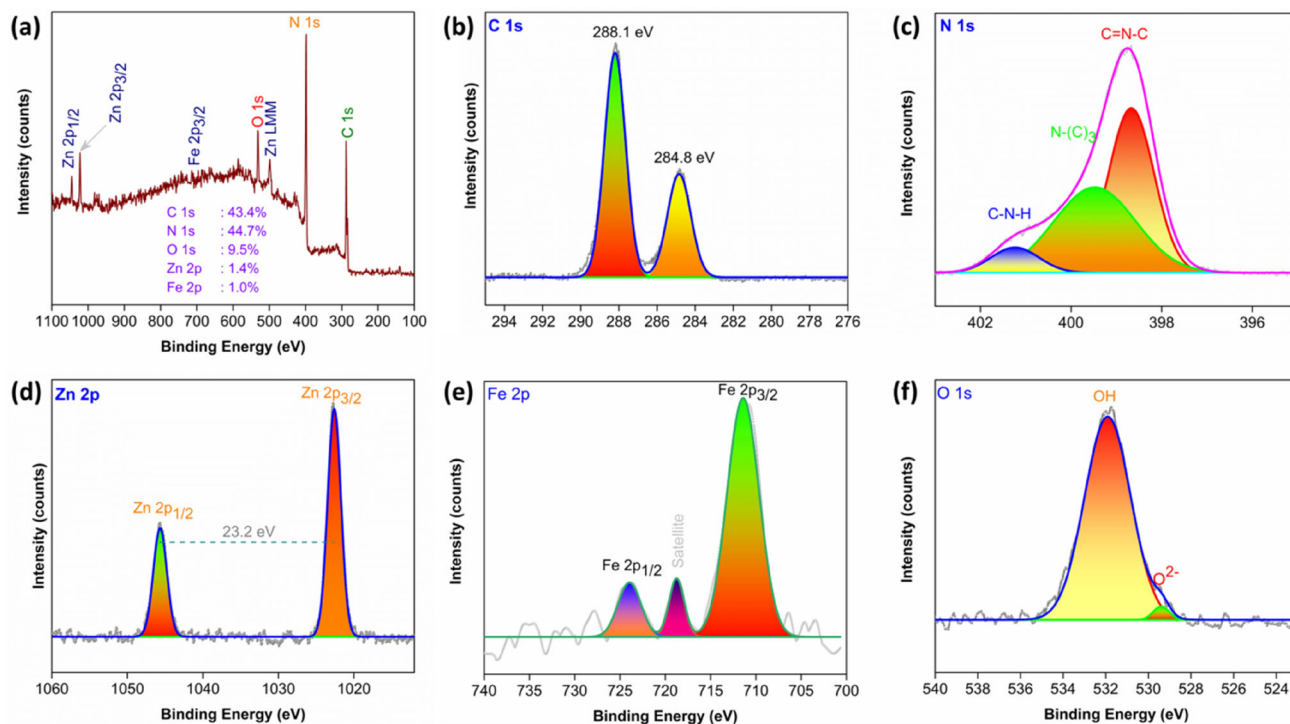


Fig. 7 **a** survey spectrum of CZF composite sample, and scan spectra of **b** C 1s, **c** N 1s, **d** Zn 2p, **e** Fe 2p, and **f** O 1s

composite existed in +2 state [51]. The Fe 2p spectrum (Fig. 7e) displays two evident peaks at 711.1 and 724 eV, which are correlated to the binding energy value of Fe 2p_{3/2} and Fe 2p_{1/2}, respectively [49]. The O 1s spectrum (Fig. 7f) for GZF composite displays two peaks at 529.3 and 531.8 eV, which are corroborated with the presence of lattice oxygen and surface OH groups, respectively [49]. Nevertheless, the peak intensities of Fe 2p are relatively very low, confirms that Fe₂O₃ present in the GZF composite is

very low. The XPS results obviously demonstrate that the synthesized GZF composite is heterostructure with strong interaction between the g-C₃N₄ and metal oxides (Fe₂O₃ and ZnO) thus enhances the migration of electron–hole pairs as well as the photocatalytic performance of the GZF composite.

The photocatalytic performance of the GCN, GZ, and GZF was estimated by the MB dye (30 mg/L) degradation under visible light irradiation. Figure 8a displays the concentration changes of MB under

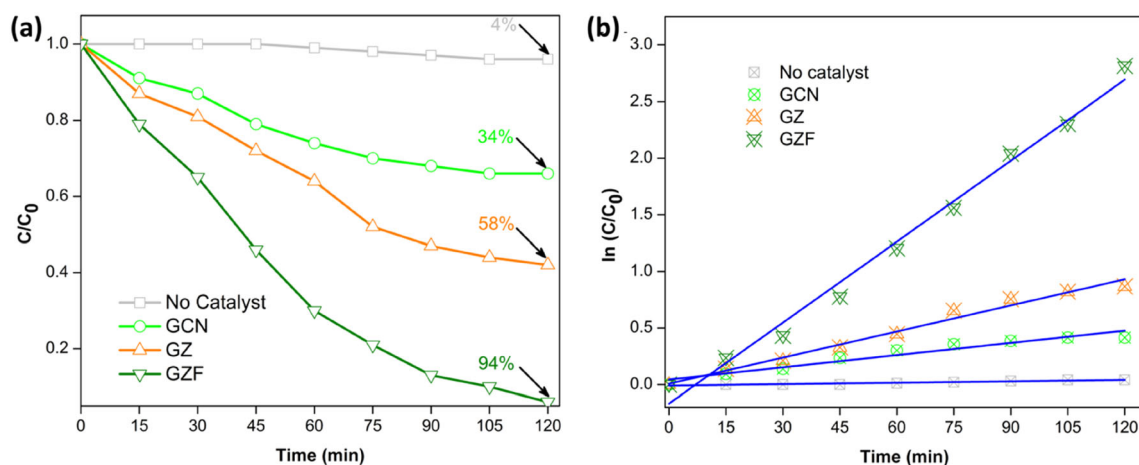


Fig. 8 **a** The degradation efficiency (C/C_0) and **b** kinetic rates of GCN, GZ, and GZF composites for photocatalytic performance of MB dye under visible irradiation

irradiation for different time intervals. After 120 min irradiation, GZF catalyst revealed superior performance with almost complete dye degradation which is higher than GCN and GZ. The result clearly indicates the metal oxides influence the degradation efficiency of $g\text{-C}_3\text{N}_4$ under visible light irradiation. Moreover, GZ catalyst shows better dye degradation performance than pristine GCN while lesser performance than GZF. The GZF offers a platform for the rapid electron transfer of the photogenerated charge carriers from $g\text{-C}_3\text{N}_4$ to metal oxides, which avoids their charge recombination and enhances their lifetime [52]. Moreover, the GZF leads the superior photocatalytic activity with the maximum MB dye degradation efficiency up to 94% than ZF (58%) and GCN (34%). To verify the rate of MB degradation, pseudo-first-order kinetic model was adopted.

$$\ln(C/C_0) = -kT,$$

where k is pseudo-first-order rate constant (min^{-1}), C_0 is the initial concentration of MB and C is the concentration of MB at time (t).

Figure 8b displays the pseudo-first-order kinetics of MB degradation with the GCN, GZ, and GZF. The MB dye degradation profiles are well-defined by pseudo-first-order kinetics, with the correlation coefficients of 0.98 ($R^2 = 98$). The kinetic constants of GCN, GZ, and GZF were found to be 0.0036, 0.0077, and 0.023 min^{-1} , respectively. Fascinatingly, the MB degradation rate on GZF was 6.6-fold and 3.1-fold higher than those on GZ and GCN, respectively. The enhanced photocatalytic performance of GZF is due to the synergistic catalytic effect between metal

oxides (ZnO and Fe_2O_3) and $g\text{-C}_3\text{N}_4$ increases electron transfer and reduces recombination [53].

TOC is one of the key analytical techniques to confirm complete mineralization of the MB dye in the aqueous medium. TOC removal of MB solution by GCN, GZ, and GZF photocatalysts was analysed under the similar condition, as shown in Fig. 9a. The GZF composite photocatalysts showed a maximum efficiency with TOC removal of 74.72% after 120 min irradiation, which is higher than GCN (28.69%) and GZ (51.81%) photocatalysts. Obviously, TOC results confirmed that the integration ZnO and Fe_2O_3 nanoparticles with GCN enhanced the MB degradation due to synergistic effect of both metal oxides and GCN nanostructures.

The radical scavengers were introduced to explore the trap specific reactive species on the active moieties involved in photocatalytic degradation of MB dye (Fig. 9b). 1,4-benzoquinone (BQN), isopropanol (IPA) and disodium ethylenediaminetetraacetate ($\text{Na}_2\text{-EDTA}$) served as trapping agents for superoxide ($\cdot\text{O}_2^-$) radical and hydroxyl ($\cdot\text{OH}$) radical and surface generated holes (h^+), respectively [54]. In a trapping-free reaction, GZF photocatalysts displayed the MB dye maximum degradation efficiency of 94% after 120 min irradiation and thus GZF photocatalysts was chosen for radical scavenging study. The photodegradation rate of MB by GZF photocatalysts was inhibited after the addition of specific scavenger species suggesting that the free radical such as $\cdot\text{OH}$, $\cdot\text{O}_2^-$, and h^+ are produced during the MB dye degradation process. The degradation rate decreased slightly with decrease in the addition of BQN,

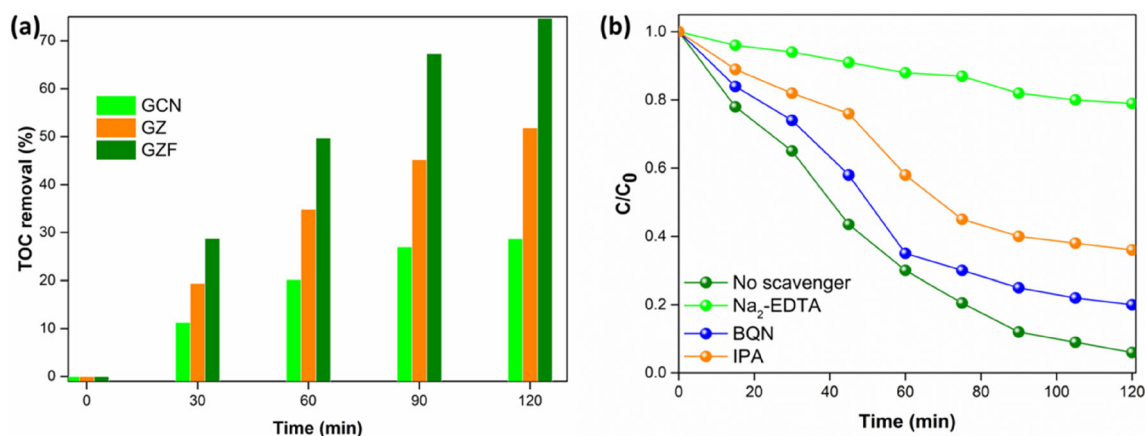


Fig. 9 a TOC removal percentage of prepared photocatalysts and b Trapping experiments of active species during degradation of MB on GZF composite

representing that $\cdot\text{O}_2^-$ has inhibited the MB degradation. When introduction of IPA, the rate of degradation significantly decreased compared to BQN, indicating that $\cdot\text{OH}$ radicals strongly prevent the MB degradation. Unfortunately, very low degradation rate was observed after addition of $\text{Na}_2\text{-EDTA}$, suggesting that the surface generated holes not actively contributing in photodegradation process of MB dye.

The impact of solution pH on the photocatalytic activity for the MB over GZF is explored by varying pH value from 3 to 11 in a 50 mL of dye solution with 50 mg/L dye concentration (Fig. 10a). The maximum MB degradation was observed at higher pH (pH 11) value than lower pH. At higher pH, catalyst surface gains negative charge from OH^- , which electrostatically attracts the cationic MB dye molecules that lead to increase the MB dye degradation [55]. In contrast, at lower solution pH, the positively charged catalyst surface from excess of H^+ ions, electrostatically oppose the cationic MB dye molecules, which results in lower degradation efficiency. Besides, at higher pH, OH^- ions can yield hydroxyl ($\cdot\text{OH}$) radicals that further elicits the rate of dye degradation.

The influence of initial MB dye concentration on the degradation performance of the GZF composite photocatalyst was examined by changing the dye concentration from 10 to 50 mg/L with the catalyst dosage of 50 mg/50 mL at pH 7.2 (Fig. 10b). The MB degradation increases with increasing initial dye concentration up to 30 mg/L, which is the maximum degradation efficiency. At a lower initial dye concentration, lesser amount of dye was adsorbed on the surface of catalyst, while at higher dye concentration, decrease in diffusion of light photon or suppressing

path distance of photons was observed leading to poor dye degradation performance [56, 57].

The effect of GZF dosage on degradation of MB was studied with different photocatalyst dosage starting from 30 to 70 mg/50 mL, as shown in Fig. 10c. The photocatalytic performance of GZF hybrid gradually increased with the photocatalyst dose up to 50 mg/50 mL, and then MB degradation rate decreased. The maximum MB degradation was found to be 50 mg/50 mL. The reduction of MB degradation above 50 mg/50 mL is due to the increase in turbidity that leads to minimization of the light penetration and non-uniform scattering of the light intensity resulting in decreased performance of the photocatalyst [58].

From the concern of practical application, the reusability of catalyst plays a key role in the dye removal process. Henceforward, the five consecutive cycles were performed for photocatalytic degradation of MB under visible light irradiation (Fig. 11a). As shown in Fig. 11a, there was no significant change observed photodegradation performance of GZF composite even after the five consecutive cycles, which confirms that the photostability and reusability of GZF composite. The superior photo-stability of GZF composite could be associated with the chemical stability and improved charge separations which inhibits the photo-corrosion [59]. Moreover, the high photostability can be attributed to the better anti-photocorrosion of GZF composites [26]. To further confirm the stability of GZF composite, photocatalyst was collected after 5 consecutive cycles and XRD was performed and compared with the XRD pattern results of the sample before photocatalytic activity.

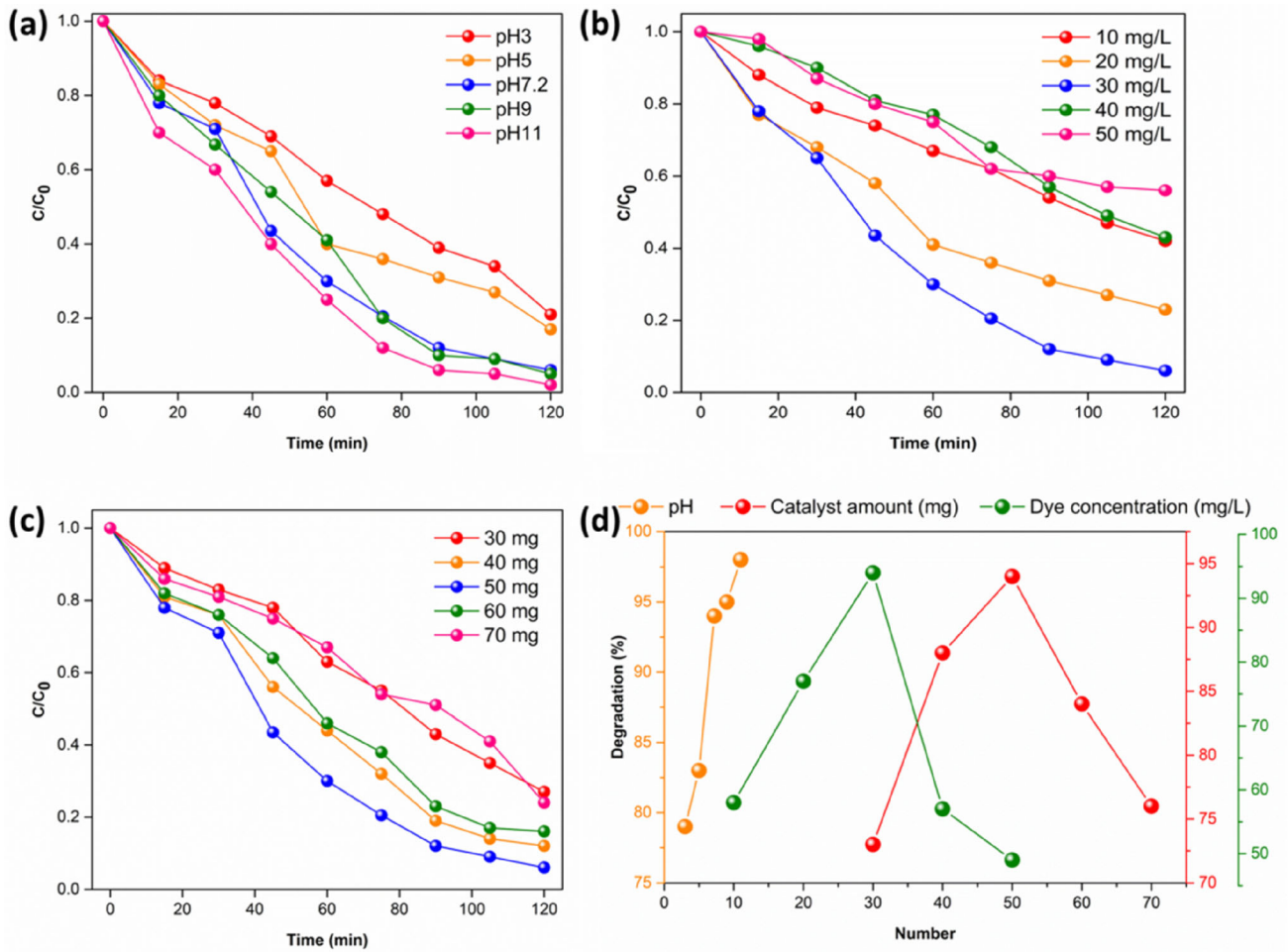


Fig. 10 Effects of **a** solution pH, **b** dosage of photocatalyst, **c** initial dye concentration, and **d** comparison of different parameters of degradation percentage of MB dye on GZF composite

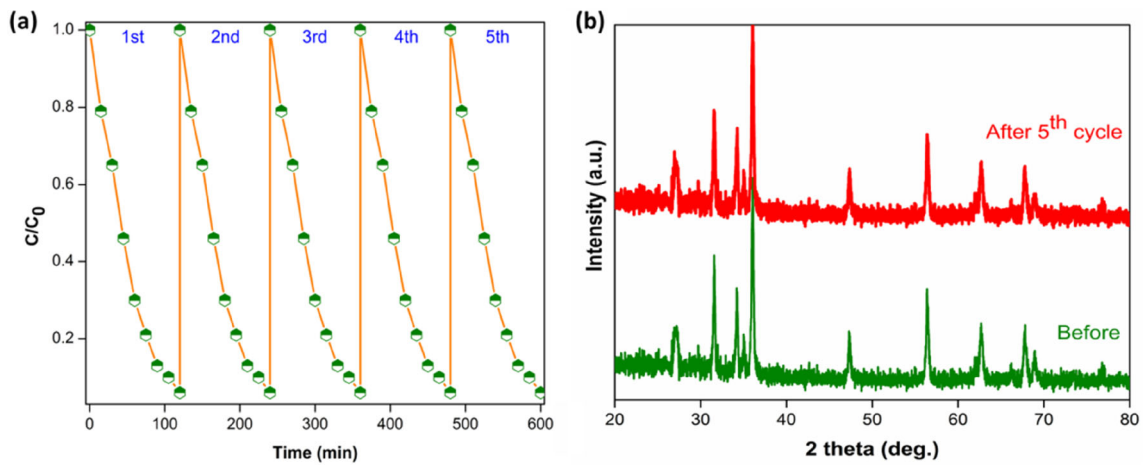


Fig. 11 **a** Stability of GZF composite by photocatalytic performance of MB solutions and **b** XRD pattern of the GZF composite after 5th cycle

As shown in Fig. 11b, there are no significant changes observed in the XRD pattern of the photocatalyst before and after the use. This indicates the GZF composite is highly stable even under visible light irradiation.

The heterostructures based on $g\text{-C}_3\text{N}_4$ composites effectively suppresses the rate of recombination which encourages the ion transportation resulting in enhanced photocatalytic performances under visible light irradiation [60–62]. The photocatalytic mechanism of GZF composites can be explained based on the mechanism provided by Di et al. [53] and schematically represented in Fig. 12a. Under visible light irradiation, initially, the $g\text{-C}_3\text{N}_4$ and metal oxides (ZnO and Fe_2O_3) can produce photogenerated electrons-hole pairs.

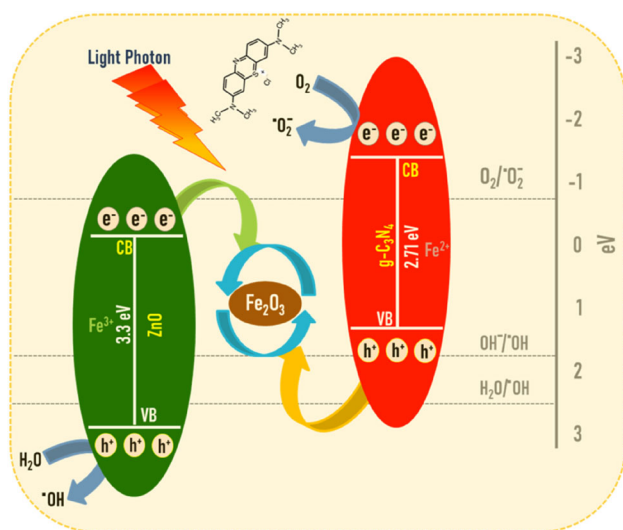
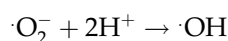
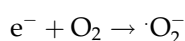
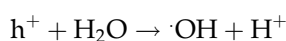
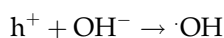
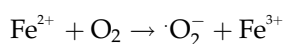
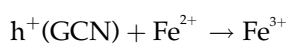


Fig. 12 Schematic representation of the possible photocatalytic mechanism in GZF composite under visible light irradiation

It is important that Fe_2O_3 acted as the redox center, revealing dual-functions including promotion of electron–hole pairs separation and generating extra reactive oxygen species (ROS). Finally, the ROS can constantly degrade MB in the form of H_2O and CO_2 , etc.



In summary, the GZF composite showed an enhanced photocatalytic performance under visible light irradiation than individual constituents which may be attributed to the following reasons; 1. Composite catalyst accelerates the rapid charge transfer, 2. The energy gap of the composite is low than the other catalysts, which also offers quick charge transfer, and 3. Composite catalysts effectively reduces the carrier recombination which leads to superior catalytic performance.

The photocatalytic performance of GZF composites is compared with $g\text{-C}_3\text{N}_4$ -based binary and ternary composites are given in Table 1. The result clearly indicates the GZF composite demonstrated outstanding photocatalytic efficacy for the degradation of MB. Henceforth, it can be believed that the composite of $g\text{-C}_3\text{N}_4$ with metal oxides will be a potential candidate for applications in dye removal from an aqueous system.

4 Conclusions

The $g\text{-C}_3\text{N}_4/\text{ZnO}/\text{Fe}_2\text{O}_3$ (GZF) composite catalyst was successfully prepared by a simple calcination method for the degradation of MB under visible light irradiation. Analytical characterisation using XRD, FTIR, UV–Vis, SEM and EDS analysis were performed to investigate the structural, optical and morphology characteristics of the GCN, GZ and GZF composites. The redshift and reduced energy gap were observed after the incorporation of metal oxides in the $g\text{-C}_3\text{N}_4$. Moreover, the GZF composite displayed enhanced photocatalytic performance for MB degradation, photostability and reusability than GCN and GZ under visible light irradiation. The results confirmed the metal oxides containing $g\text{-C}_3\text{N}_4$ catalyst effectively enhanced the electron-hole pair and remarkably reduce the recombination that leads improved dye degradation. Foremost, this investigation thus provides a new way to develop high

Table 1 Comparison of photocatalytic performance for degradation with other g-C₃N₄/ZnO, g-C₃N₄/Fe₂O₃, and g-C₃N₄/ZnO/Fe₂O₃-based composites

Sample	Catalyst concentration (mg/L)	Initial dye concentration (mg/L)	Time of irradiation (min)	Percentage of degradation (%)	References
g-C ₃ N ₄ /Fe ₂ O ₃	10	2.5	180	91	[63]
g-C ₃ N ₄ -ZnO	100	10	120	90	[64]
g-C ₃ N ₄ /ZnO	200	20	30	85.7	[65]
g-C ₃ N ₄ /Cr-ZnO	100	10	90	93	[66]
S-g-C ₃ N ₄ /Cu-ZnO	50	10	90	93	[67]
g-C ₃ N ₄ /α-Fe ₂ O ₃	50	18	150	80.93	[68]
g-C ₃ N ₄ /Fe ₂ O ₃	100	10	90	70	[69]
g-C ₃ N ₄ /ZnO/Fe ₂ O ₃	10	30	150	83.35	[32]
g-C ₃ N ₄ /ZnO/Fe ₂ O ₃	50	30	120	94	This study

performing photocatalytic material for the degradation of organic dye pollutants.

Author contributions

Conceptualization: [KS,VM]; Methodology: [KS,VCAP,KMG]; Formal analysis and investigation: [RG,GSL]; Writing—original draft preparation: [RG]; Writing—review and editing: [RG,GSL], Resources: [GSL], Supervision: [VM].

Funding

The authors have not disclosed any funding.

Data availability

The data that support the findings of this study are available from the corresponding author on reasonable request.

Declarations

Conflict of interest The author declares no competing interests.

References

1. J. He, D.W. Shao, L.C. Zheng, L.J. Zheng, D.Q. Feng, J.P. Xu, X.H. Zhang, W.C. Wang, W.-H. Wang, F. Lu, H. Dong, Y.H. Cheng, H. Liu, R.K. Zheng, *Appl. Catal. B Environ.* **203**, 917–926 (2017)
2. Z. Zhang, K. Liu, Y. Bao, B. Dong, *Appl. Catal. B Environ.* **203**, 599–606 (2017)
3. S. Kamal, S. Balu, S. Palanisamy, K. Uma, V. Velusamy, T.C.K. Yang, *Results Phys.* **12**, 1238–1244 (2019)
4. X. Chen, Z. Wu, D. Liu, Z. Gao, *Nanoscale Res. Lett.* **12**, 143 (2017)
5. H. Hu, Y. Lin, Y.H. Hu, *Catal. Today* **341**, 90–95 (2020)
6. X. Wang, K. Maeda, A. Thomas, K. Takanebe, G. Xin, J.M. Carlsson, K. Domen, M. Antonietti, *Nat. Mater.* **8**, 76–80 (2009)
7. C. Liu, W. Ma, J. Chen, Z. Mao, D. Wang, *J. Mater. Sci.: Mater. Electron.* **32**, 25033–25044 (2021)
8. A.A. Yadav, S.-W. Kang, Y.M. Hunge, *J. Mater. Sci.: Mater. Electron.* **32**, 15577–15585 (2021)
9. Y. Li, Y. Sun, W. Ho, Y. Zhang, H. Huang, Q. Cai, F. Dong, *Sci. Bull.* **63**, 609–620 (2018)
10. D. Mittal, D.P. Dutta, *J. Mater. Sci.: Mater. Electron.* **32**, 18512–18543 (2021)
11. A.H. Kianfar, M.A. Arayesh, *J. Environ. Chem. Eng.* **8**, 103640 (2020)
12. I. Khan, K. Saeed, I. Zekker, B. Zhang, A.H. Hendi, A. Ahmad, S. Ahmad, N. Zada, H. Ahmad, L.A. Shah, T. Shah, I. Khan, *Water* **14**, 242 (2022)
13. H. Li, Y. Zhao, C. Yin, L. Jiao, L. Ding, *Colloids Surf. A Physicochem. Eng. Asp.* **572**, 147–151 (2019)

14. S. Zhang, P. Gu, R. Ma, C. Luo, T. Wen, G. Zhao, W. Cheng, X. Wang, *Catal. Today* **335**, 65–77 (2019)
15. M. Ismael, *Chem. Phys. Lett.* **739**, 136992–137002 (2020)
16. Y. Ren, D. Zeng, W.-J. Ong, *Chin. J. Catal.* **40**, 289–319 (2019)
17. S. Tonda, S. Kumar, S. Kandula, V. Shanker, *J. Mater. Chem. A* **2**, 6772–6780 (2014)
18. Z. Jiang, C. Zhu, W. Wan, K. Qian, J. Xie, *J. Mater. Chem. A* **4**, 1806–1818 (2016)
19. Y.-X. Sun, Y.-P. Yuan, L.-C. Qiu, X. Jiang, A.-J. Xie, Y.-H. Shena, J.-H. Zhu, *Dalton Trans.* **41**, 6756–6763 (2012)
20. T. Senasu, T. Chankhanittha, K. Hemavibool, S. Nanan, *Mater. Sci. Semicond. Process.* **123**, 105558–105572 (2021)
21. T. Sansenya, N. Masri, T. Chankhanittha, T. Senasu, J. Piriyanon, S. Mukdasai, S. Nanan, *J. Phys. Chem. Solids* **160**, 110353 (2021)
22. S. Kakarndee, S. Nanan, *J. Environ. Chem. Eng.* **6**, 74–94 (2018)
23. M. Gayathri, M. Sakar, E. Satheeshkumar, E. Sundaravadivel, *J. Mater. Sci.: Mater. Electron.* **33**, 9347–9357 (2022)
24. S. Balu, S. Velmurugan, S. Palanisamy, S.-W. Chen, V. Velusamy, T.C.K. Yang, E.-S.I. El-Shafey, *J. Taiwan Inst. Chem. Eng.* **99**, 258–267 (2019)
25. R. Chalasani, S. Vasudevan, *ACS Nano* **7**, 4093–4104 (2013)
26. Z. Wang, Y. Fan, R. Wu, Y. Huo, H. Wu, F. Wang, X. Xu, *RSC Adv.* **8**, 5180–5188 (2018)
27. D. Xiao, K. Dai, Y. Qu, Y. Yin, H. Chen, *Appl. Surf. Sci.* **358**, 181–187 (2015)
28. Y. Wang, X. Li, Y. Yang, J. Yang, N. Zhang, X. Wu, X. Li, *J. Mater. Sci.: Mater. Electron.* **31**, 5187–5197 (2020)
29. Y. Sheng, Z. Wei, H. Miao, W. Yao, H. Li, Y. Zhu, *Chem. Eng. J.* **370**, 287–294 (2019)
30. J.X. Sun, Y.P. Yuan, L.G. Qiu, X. Jiang, A.J. Xie, Y.H. Shen, *Dalton Trans.* **41**, 6756–6763 (2012)
31. A. Khan, U. Alam, W. Raza, D. Bahnemann, M. Muneer, *J. Phys. Chem. Solids* **115**, 59–68 (2018)
32. Z. Wu, X. Chen, X. Liu, X. Yang, Y. Yang, *Nanoscale Res. Lett.* **14**, 147 (2019)
33. C. Lu, P. Zhang, S. Jiang, X. Wu, S. Song, M. Zhu, Z. Lou, Z. Li, F. Liu, Y. Liu, Y. Wang, Z. Le, *Appl. Catal.: B Environ.* **200**, 378–385 (2017)
34. P. Praus, L. Svoboda, R. Dvorský, M. Reli, *Ceram. Int.* **44**, 3837–3846 (2018)
35. C.K. Fan, Q. Feng, G.Q. Xu, J. Lv, Y. Zhang, J.Q. Liu, Y.Q. Qin, Y.C. Wu, *Appl. Surf. Sci.* **427**, 730–738 (2017)
36. Y.C. Zhao, D.L. Yu, H.W. Zhou, Y.J. Tian, O. Yanagisawa, *J. Mater. Sci.* **40**, 2645–2647 (2005)
37. Z. Wang, H. Zhang, L. Zhang, J. Yuan, S. Yan, C. Wang, *Nanotechnology* **14**, 11–15 (2003)
38. X. Li, J. Zhang, L. Shen, Y. Ma, W. Lei, Q. Cui, G. Zou, *Appl. Phys. A* **94**, 387–392 (2009)
39. Z. Zhu, P. Huo, Z. Lu, Y. Yan, Z. Liu, W. Sh, H. Dong, *Chem. Eng. J.* **331**, 615–625 (2018)
40. Z. Yang, J. Yan, J. Lian, H. Xu, X. She, H. Li, *Chem. Select.* **1**, 5679–5685 (2016)
41. A. Behera, D. Kandi, S.M. Majhi, S. Martha, K. Parida, *Beilstein J. Nanotechnol.* **9**, 436–446 (2018)
42. N. Mao, *Sci. Rep.* **9**, 12383 (2019)
43. L.A.L. Thi, M.M. Neto, T.P. Van, T.N. Ngoc, T.M.N. Thi, X.S. Nguyen, C.T. Nguyen, *Adv. Mater. Sci. Eng.* **2021**, 6651633 (2021)
44. C. Schlumberger, M. Thommes, *Adv. Mater. Interface* **8**, 2002181 (2021)
45. G. Greczynski, L. Hultman, *Prog. Mater. Sci.* **107**, 100591 (2020)
46. P. Sharma, P.P. Sarngan, A. Lakshmanan, D. Sarkar, *J. Mater. Sci: Mater. Electron.* **33**, 9116–9125 (2022)
47. T. He, Y. Wu, C. Jiang, Z. Chen, Y. Wang, G. Liu, Z. Xu, G. Ning, X. Chen, Y. Zhao, *PLoS ONE* **15**, e0237389 (2020)
48. X. Yang, F. Qian, G. Zou, M. Li, J. Lu, Y. Li, M. Bao, *Appl. Catal. B* **193**, 22 (2016)
49. Q. Xu, B. Zhu, C. Jiang, B. Cheng, J. Yu, *Sol. RRL* **2**, 1800006 (2018)
50. N. Kumaresan, M. Maria AngelinSinthiya, M. Praveen Kumar, S. Ravichandran, R. Ramesh Babu, K. Sethurman, K. Ramamurthi, *Arab. J. Chem.* **13**, 2843 (2020)
51. D.S. Rahman, S.K. Pal, S.S. Singha, S. Kundu, S. Basu, S.K. Ghosh, *Mater. Adv.* **1**, 2897–2907 (2020)
52. Y.P. Zhu, M. Li, Y.L. Liu, T.Z. Ren, Z.Y. Yuan, *J. Phys. Chem. C* **118**, 10963–10971 (2014)
53. G. Di, Z. Zhu, H. Zhang, J. Zhu, Y. Qiu, D. Yin, S. Küppers, *J. Colloid Interface Sci.* **538**, 256–266 (2019)
54. M. Zhou, X. Tian, H. Yu, Z. Wang, C. Ren, L. Zhou, Y.-W. Lin, L. Dou, *ACS Omega* **6**, 26439–26453 (2021)
55. I.-H. Tseng, Y.-M. Sung, P.-Y. Chang, C.-Y. Chen, *Polymers* **11**, 146 (2019)
56. H. Osman, Z. Su, X. Ma, *Environ. Chem. Lett.* **15**, 435–441 (2017)
57. R.C. Pawar, Y. Son, Y.J. Kim, S.H. Ahn, C.S. Lee, *Curr. Appl. Phys.* **16**, 101–108 (2018)
58. M.A. Bajiri, A. Hezam, K. Namratha, R. Viswanath, Q.A. Drmash, H.S.B. Naik, K. Byrappa, *J. Environ. Chem. Eng.* **7**, 103412 (2019)
59. X. Zhong, M. Jin, H. Dong, L. Liu, L. Wang, H. Yu, S. Leng, G. Zhuang, X. Li, W. Wang, *J. Solid. State. Chem.* **220**, 54–59 (2019)
60. A. Alsalme, A.H. Galal, E.F. El-Sherbeny, A. Soltan, M.F. Abdel-Messih, M.A. Ahmed, *Diam. Relat. Mater.* **122**, 108819 (2022)

61. H.S.M. Abd-Rabboh, A.H. Galal, R.A. Aziz, M.A. Ahmed, RSC Adv. **11**, 29507–29518 (2021)
62. M. Benaissa, N. Abbas, S.A. Arni, N. Elboughdiri, A. Moumen, M.S. Hamdy, H.S.M. Abd-Rabboh, A.H. Galal, M.G. Al-Metwaly, M.A. Ahmed, Opt. Mater. **118**, 111237 (2021)
63. M.R. Shenoy, S. Ayyasamy, V. Bhojan, R. Swaminathan, N. Raju, P. Senthil Kumar, M. Sasikumar, G. Kadarkarai, S. Tamilarasan, S. Thangavelu, J. Suryakanth, M.V. Reddy, J. Mater. Sci.: Mater. Electron. **32**, 4766–4783 (2021)
64. D.R. Paul, S. Gautam, P. Panchal, S.P. Nehra, P. Choudhary, A. Sharma, ACS Omega **5**, 3828–3838 (2020)
65. F. Yu, Y. Li, Z. Liu, D. Nan, B. Wang, L. He, J. Zhang, X. Tang, Y. Liu, Appl. Phys. A **127**, 818 (2021)
66. M.A. Qamar, S. Shahid, M. Javed, S. Iqbal, M. Sher, M.B. Akbar, J. Photochem. Photobiol. A **401**, 112776 (2020)
67. M. Javed, M.A. Qamar, S. Shahid, H.O. Alsaab, S. Asif, RSC Adv. **11**, 37254–37267 (2021)
68. T. Wang, M. Huang, X. Liu, Z. Zhang, Y. Liu, W. Tang, S. Bao, T. Fang, RSC Adv. **9**, 29109–29119 (2019)
69. M.A. Karimi, M. Iliyati, M. Atashkadi, M. Ranjbar, A. Habibi-Yangjeh, J. Chin. Chem. Soc. **67**, 2032–2041 (2020)

Publisher's Note Springer Nature remains neutral with regard to jurisdictional claims in published maps and institutional affiliations.